ELSEVIER

Journal of Power Sources 102 (2001) 21–28

JOURNAL OF POWER SOURCES

www.elsevier.com/locate/jpowsour

Effect of Co doping in $LiMn_2O_4$

C.H. Shen[a], R.S. Liu[a,*], R. Gundakaram[a], J.M. Chen[b], S.M. Huang[c], J.S. Chen[c], C.M. Wang[c]

[a]*Department of Chemistry, National Taiwan University, Rossevelt Road, Section 4, Taipei, Taiwan, ROC*
[b]*Synchrotron Radiation Research Center, Hsinchu, Taiwan, ROC*
[c]*SYNergy ScienTech Corporation, Hsinchu, Taiwan, ROC*

Received 11 January 2001; accepted 13 March 2001

Abstract

Lithium transition-metal oxides $Li(Mn_{2-x}Co_x)O_4$ ($0 \leq x \leq 0.5$) are synthesized by solid state reaction. X-ray and electrochemical data show that the replacement of Mn^{3+} (d^4) ions by Co^{3+} (d^6) in the octahedral framework of the spinel eliminates the local disorder present in the lattice around the $[Mn^{3+}O_6]$ octahedra. The capacity loss observed in the undoped $Li/LiMn_2O_4$ cell is about 25% after 20 cycles, whereas that for the $x = 0.1$ and 0.2 doped spinel materials is about 0.48 and 1%, respectively. The good capacity retention of $Li(Mn_{2-x}Co_x)O_4$ ($0.1 \leq x \leq 0.5$) electrode is attributed to the stabilization of the spinel structure by Co doping for Mn ion sites. The chemical substitution of Co^{3+} for Mn^{3+} in $LiMn_2O_4$ improves the efficiency in maintaining electrochemical capacity over a large number of cycles without sacrificing initial reversible capacity at room temperature.

Keywords: Solid state reaction; $Li(Mn_{2-x}Co_x)O_4$; Chemical substitution; Capacity

1. Introduction

High voltage cathode materials for use in lithium based secondary battery systems have been of considerable interest in recent years. Lithium transition-metal (V, Cr, Mn, Co, Ni) oxides, which are used as positive electrodes in secondary lithium batteries, have been extensively studied over the past two decades [1–3]. In all lithium battery systems, energy storage is associated with a reversible lithium intercalation into the positive electrode materials. Commercial lithium cells use lithium cobalt oxide cathodes and the high cost of this material has prompted the design and synthesis of alternate insertion hosts. Among these alternatives, manganese oxides have been found to be promising in terms of specific energy, non-toxicity, and low cost. Lithium spinel $LiMn_2O_4$ is the most promising candidate for innovative lithium-ion (rocking chair) batteries. It is thought that lithium manganese oxides batteries will be used in cellular telephones, notebook PCs and electrical vehicles [4–7].

Some problems for commercial application of $LiMn_2O_4$ are rechargeable capacity and poor cyclability of the charge–discharge process in the 4-V region. The major factors responsible for the capacity loss at elevated temperatures are as follows [8,9]: (i) the more stable one-phase structure in the low-voltage region transforms to an unstable two phase on the high-voltage region; (ii) Mn^{3+} ions in $LiMn^{3+}Mn^{4+}O_4$ cathode materials undergo a self-redox reaction to Mn^{2+} and Mn^{4+} at high voltages, which induces capacity loss due to a loss of the cathode; the Mn^{2+} so generated irreversibly dissolves in the electrolyte and increases in resistance of the cell; (iii) the decomposition of the electrolyte solution at the electrode at high voltage causes lattice instability of $LiMn_2O_4$. This metal oxide shows cubic $Fd\bar{3}m$ symmetry at room temperature, with an average manganese valence of 3.5. The Mn exists in Mn^{4+} ($t_{2g}^3e_g^0$) and Jahn–Teller active Mn^{3+} ($t_{2g}^3e_g^1$) configurations. Several studies have been aimed at improving the material properties of $LiMn_2O_4$ and at improving its efficiency in maintaining electrochemical capacity over a large number of cycles without sacrificing initial reversible capacity and also its performance at room temperature [10,11]. Doping the Mn (16d) sites with a trivalent cation or a cation with lesser valence is a possibility, because it reduces the Mn^{3+} content and stabilizes the cubic structure in the face of Mn^{3+} Jahn–Teller distortion [12–18]. Guohua et al. [17] have shown that the substitution of M ions at the Mn site, $Li(Mn, M)_2O_4$ (M = Cr, Co and Ni), increases the average ionic valence of Mn, and thus decreases the number of Jahn–Teller Mn^{3+}

* Corresponding author. Tel.: +886-2-23690152/ext. 148; fax: +886-2-23636359.
E-mail address: rsliu@ccms.ntu.edu.tw (R.S. Liu).

0378-7753/01/$ – see front matter
PII: S0378-7753(01)00765-0

ions. Considering both cycle-life and capacity density, $LiCo_{1/6}Mn_{11/6}O_4$ shows good cycle performance with a specific energy of 370 Wh kg^{-1} at the 300th cycle. The improvement in cycling performance is attributed to stabilization of the spinel structure by doped metal cations.

In this paper, we report the synthesis of $Li(Mn_{2-x}Co_x)O_4$ ($0 \leq x \leq 0.5$), wherein Mn has been partially replaced with Co ions to improve the cycle performance of $LiMn_2O_4$ spinel materials.

2. Experimental

2.1. Synthesis of $Li(Mn_{2-x}Co_x)O_4$

Samples of the system $Li(Mn_{2-x}Co_x)O_4$ ($0 \leq x \leq 0.5$) were synthesized by solid state reaction of Li_2CO_3, MnO_2 and Co_3O_4. Well ground mixtures of the starting materials were heated at 800°C in air for 24 h, followed by two treatments each of 24 h at 800°C with intermediate grindings. The process was repeated to minimize the impurities Mn_2O_3 and Li_2MnO_3. Powder X-ray diffraction (XRD) analyses were carried out with a SCINTAG (X1) diffractometer (Cu Kα radiation, $\lambda = 1.5406$ Å) at 40 KeV and 30 mA. Data for the Rietveld refinement were collected in the 2θ range 15–120° with a step size of 0.02° and a count time of 10 s per step. The GSAS program [19] was used for the Rietveld refinement in order to obtain information about the crystal structures of $Li(Mn_{2-x}Co_x)O_4$. In all cases, the XRD patterns could be indexed on the basis of a cubic cell.

2.2. SEM and BET

The scanning electron microscopy (SEM) pictures were recorded at room temperature on a Philips XL30 scanning electron microscope equipped with a field emission gun which operated at 20 kV. Compositional analyses were performed by using an EDAX-DX4 energy dispersive X-ray spectrometer (EDS). The specific surface area for each as-prepared compound was analyzed with a Micrametric ASAP 2000 instrument by the Brunauer, Emment, and Teller (BET) method in which N_2 gas adsorption was employed. Each compound was heated to 250°C and at a partial pressure of 10^{-3} Torr for 2 h to remove the adsorbed water before measurement.

2.3. Measurement of Mn valence

The valence of Mn was determined by the X-ray absorption technique. The experiments were carried out at the synchrotron radiation research center (SRRC) in Taiwan with an electron beam energy of 1.5 GeV and a maximum stored current of 240 mA. The spectra were recorded by measuring the sample current. The incident photon flux (I_0) was monitored simultaneously by a Ni mesh located after the exit slit of the monochromator. All the measurements were performed at room temperature. The reproducibility of the absorption spectra of the same sample in different experimental runs was found to be extremely good. The photon energies were calibrated to an accuracy of 0.1 eV via the known O K-edge absorption peaks of CuO.

The valence of Mn was also determined by chemical titration [20]. The samples were dissolved in an excess of 20 ml $K_2C_2O_4$ and 2 ml H_2SO_4 at ~65°C (maintained by a water bath) to reduce all Mn^{n+} to Mn^{2+} ($2 < n \leq 4$), and then the excess $C_2O_4^{2-}$ ions in the solution were determined by titration at 65°C with a standard solution of $KMnO_4$ [16]. Magnetization data were collected using a superconducting quantum interference device (SQUID) magnetometer (quantum design).

2.4. Electrochemical experiments

Electrochemical characterization was performed using coin-type cells. The method of assembling the cell was as follows. The cathode was prepared by spreading a mixture of 85 wt.% $LiMn_2O_4$, 9 wt.% acetylene black used as conductive material and 6 wt.% polyvinylidene fluoride (PVDF) dissolved in 1-methyl-2-pyrolidinone (NMP) on to aluminum foil. The prepared electrode was then put into a vacuum oven to evaporate the solvent at 110°C for several hours. Cathode disks (1/2 in.) were punched from the sheet, with an average weight of 3 mg of active material. The cell consisted of a cathode and a lithium metal anode separated by a porous polyethylene film. The electrolyte used was 1 M $LiPF_6$ in a mixture of ethylene carbonate (EC) and dimethyl carbonate (DMC) in the volume ratio of 1 EC:2 DMC. The cell was assembled in an argon-filled dry box and tested at room temperature. The charge and discharge experiments were performed with a Maccor battery cycling instrument. The cell was cycled at current density values between 0.3 and 3 mA cm^{-2} in the voltage range 2.80–4.25 V.

3. Results and discussion

3.1. X-ray diffraction study

The electrochemically inactive phase Li_2MnO_3 occurs as an impurity during the synthesis, as can be seen from Fig. 1. Li_2MnO_3 can be represented by the formula $Li(Li_{1/3}Mn_{2/3})O_2$ and belongs to the space group $C2/c$. In this compound, the Li^+ ion is located between the layers of the $Mn(Li)O_6$ octahedra. Based on the three heat treatments, the powder XRD patterns of $Li(Mn_{2-x}Co_x)O_4$ with $x = 0$–0.5 are shown in Fig. 2. The $Li(Mn_{2-x}Co_x)O_4$ ($0 \leq x \leq 0.5$) samples each have a single phase. We assume that the Co^{3+} ions substitute the Mn sites homogeneously while retaining the $Fd\bar{3}m$ space group. The peaks in each XRD pattern can be indexed on the basis of a cubic unit cell. The ideal crystal structure of $Li(Mn_{2-x}Co_x)O_4$ with a cubic cell at room temperature is

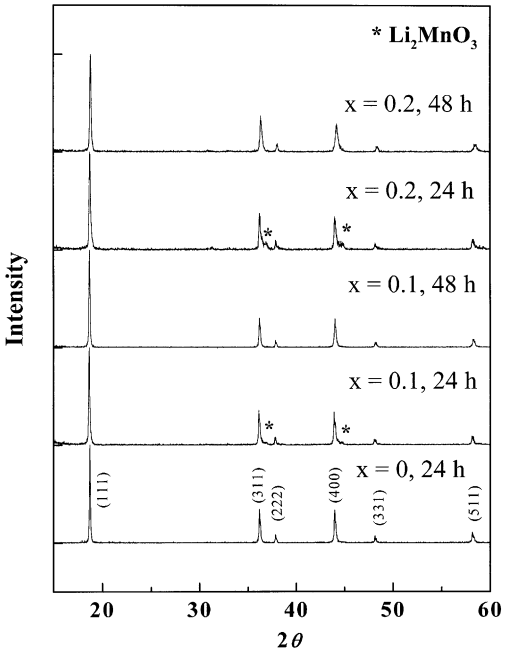

Fig. 1. X-ray powder diffraction patterns for $Li(Mn_{2-x}Co_x)O_4$ with $x = 0$, 0.1 and 0.2 sintered at 800°C in air for 24 and 48 h ($x = 0.1$ and 0.2 compositions sintered for 24 h show impurity phase Li_2MnO_3 from $Li(Mn_{2-x}Co_x)O_4$ spinel phase).

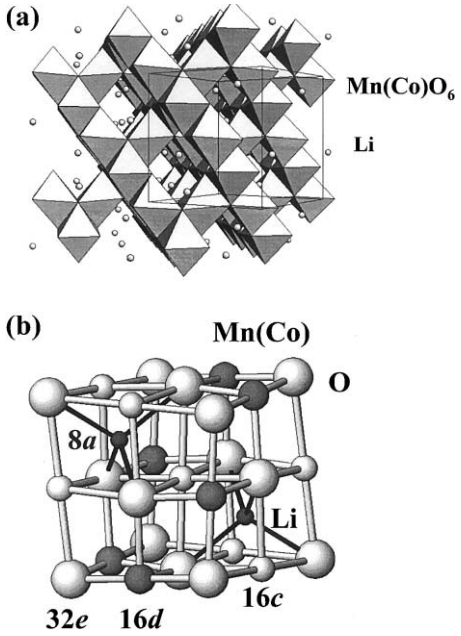

Fig. 3. (a) Ideal crystal structure of $Li(Mn_{2-x}Co_x)O_4$ with cubic cell (space group: $Fd\bar{3}m$). Unit cell is shown with a solid line. Part of each $Mn(Co)O_6$ octahedra is shaded. (b) Portion of cubic $Li(Mn_{2-x}Co_x)O_4$ spinel structure; O at 32e site, Mn(Co) at 16d site and Li at 8a site.

shown in Fig. 3. The unit cell contains 56 atoms: 8 Li, 16 Mn(Co), 32 O. The crystal structure can be described as Mn(Co) ions occupying one half of octahedral sites (16d) and Li ions present on eight of the tetrahedral sites (8a) within the cubic close-packed oxide array (32e) [21].

A perovskite symmetry was identified by observation of the reflections with the limiting condition on *hkl*: *h*, *k*, *l* either all odd or all even, with *F* centering of the unit cell, which is consistent with the results from the XRD pattern as shown in Fig. 2. We therefore kept the occupancies of the Mn(Co) sites as constant in our data refinement. The observed and calculated XRD profiles of the sample with $x = 0.1$ are shown in Fig. 4. The structural parameters of the $Li(Mn_{2-x}Co_x)O_4$ compositions at room temperature are listed in Table 1. Although all the Mn ions in the solid solution are located in the octahedral sites, Co coexists with Mn in these sites. This cause the Mn–O bond lengths to depend not only on the valence state of Mn, but also on the concentration and valence state of Co. The lattice constant *a* and the cell volume decreases with addition of Co, as shown in the inset of Fig. 4. This is due to the smaller size of the substituting Co^{3+} ion (0.545 Å for coordination number (CN) = 6, in low crystal field) as compared with the larger Mn^{3+} ion (0.645 Å for CN = 6, in low crystal field) [22]. If, however, Co^{3+} substitutes into the Mn^{4+} site (0.53 Å for CN = 6, in low crystal field) [22], an increase in the lattice constant *a* with increasing *x* in $Li(Mn_{2-x}Co_x)O_4$ will be found. Therefore, based on our results, we confirm that Co^{3+} substitutes into the Mn^{3+} sites. The Co ion has a larger binding energy (1067 KJ mol^{-1}) in CoO_6 octahedra than the Mn ion in MnO_6 octahedra (946 KJ mol^{-1}) [17], so that the Co ion prefers to substitute at the octahedral Mn site and substitutes for the Mn^{3+} ion. The formula can be written in $LiMn_1{}^{4+}Mn_{1-x}{}^{3+}Co_x{}^{3+}O_4$. We have also investigated the low temperature orthorhombic structure of $LiMn_2O_4$ by powder synchrotron diffraction and the results are reported elsewhere [23]. On the other hand, in the XRD patterns

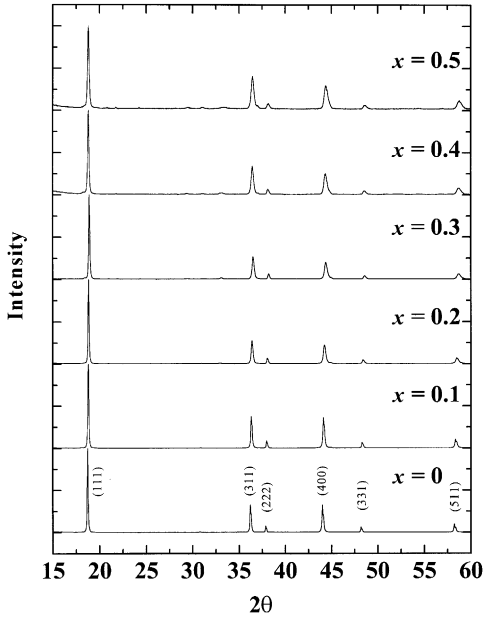

Fig. 2. X-ray powder diffraction patterns of $Li(Mn_{2-x}Co_x)O_4$ ($0 \le x \le 0.5$) samples sintered three times at 800°C in air for 24 h.

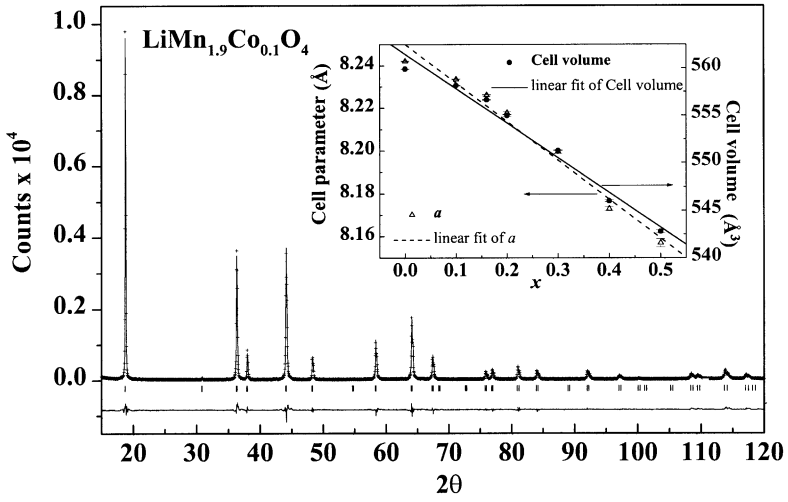

Fig. 4. Rietveld plot of $Li(Mn_{2-x}Co_x)O_4$ with $x = 0.1$ at 300 K. Experimental data points are shown as plus (+) signs. Solid line is calculated profile. Tick marks below profile indicate positions of allowed Bragg reflections. Difference plot (observed minus calculated) is shown at bottom. Basic cell parameters (a) and cell volume (V) as a function of x in $Li(Mn_{2-x}Co_x)O_4$ are shown in inset.

of the $Li(Co_{0.1}{}^{3+}Mn_{0.9}{}^{3+}Mn_{1.0}{}^{4+})O_4$ sample showing the cubic spinel structure from 300 down to 25 K, there is no peak split or broadening from room temperature to low temperature [23]. The substitution effect of Co^{3+} on the framework would be local to the 16d site, which is similar to excess Li^+ being substituted into the Mn site [24]. In $LiMn_{1.9}Co_{0.1}O_4$, the Mn^{3+} content decreases from 50 to 47% due to the change in the magnetic-ordering because of the Mn^{3+} distribution [23].

3.2. Particle size and surface area

The de-intercalation and intercalation of lithium has a significant effect on the surface of cathode materials. The morphology and particle size of the $Li(Mn_{2-x}Co_x)O_4$ ($0 \leq x \leq 0.5$) samples were observed by means of SEM and are shown in Fig. 5. An increase in the particle size with increasing Co content (from ~0.2 to ~0.8 μm of $x = 0$ and $x = 0.5$, respectively) is found. This seems to indicate that the incorporation of Co into the Mn sites can help grain growth during the sintering process [25]. The $Li(Mn_{2-x}Co_x)O_4$ ($0 \leq x \leq 0.5$) samples each have a single phase. EDS measurements have shown that the actual ratios of Mn to Co in the compositions are consistent with the nominal compositions, as can be seen from Fig. 6(a). The trend of BET results shown in Fig. 6(b) is similar that observed from SEM studies. The surface area approaches a constant value for $x > 0.4$ [25].

Table 1
Refined fractional atomic positions, unit cell parameters and reliability factors (%) of $Li(Mn_{2-x}Co_x)O_4$ having $Fd\bar{3}m$ space group at room temperature[a]

		$x = 0$	$x = 0.1$	$x = 0.2$	$x = 0.3$	$x = 0.4$	$x = 0.5$
Li	$10^2\ u_{iso}$ (Å^2)	3.3(6)	4.0(5)	2.4(6)	2.4(7)	4.6(7)	6.2(7)
Mn(Co)	$10^2\ u_{iso}$ (Å^2)	2.37(3)	2.02(3)	2.42(4)	2.42(5)	2.31(5)	2.03(6)
O	x	0.2641(2)	0.2623(2)	0.2635(2)	0.2645(3)	0.2625(3)	0.2627(3)
	$10^2\ u_{iso}$ (Å^2)	3.81(7)	3.7(1)	3.03(9)	3.2(1)	2.8(1)	2.2(1)
a	(Å)	8.2422(2)	8.2336(2)	8.2178(6)	8.1996(9)	8.173(1)	8.157(2)
Volume	(Å^3)	559.93(2)	558.17(3)	554.98(7)	551.3(1)	546.0(1)	542.8(2)
R_p	(%)	9.78	8.99	10.16	10.99	10.06	7.87
R_{wp}	(%)	12.91	12.18	13.96	15.20	14.30	10.60
χ^2	(%)	1.08	1.32	1.65	2.35	3.28	3.68
Li–O × 6	(Å)	1.983(2)	1.959(2)	1.971(3)	1.981(4)	1.947(4)	1.946(4)
Mn–O × 6	(Å)	1.953(1)	1.962(1)	1.950(2)	1.938(2)	1.946(2)	1.941(2)
Mn–Mn × 6	(A)	2.91406(6)	2.91101(7)	2.9055(2)	2.8990(2)	2.8897(4)	2.8840(5)
O–Li–O	o	109.471(3)	109.471(2)	109.471(3)	109.471(4)	109.471(5)	109.471(7)
O–Mn–O	o	83.07(9)	83.92(9)	83.31(1)	82.8(1)	83.8(1)	83.7(2)
O–Mn–O	o	180	180	180	180	180	180
O–Mn–O	o	96.93(9)	96.08(9)	96.7(1)	97.2(1)	96.2(1)	96.3(2)

[a] The atomic positions are Li: (0.125, 0.125, 0.125), Mn(Co): (0.5, 0.5, 0.5), O: (x, x, x).

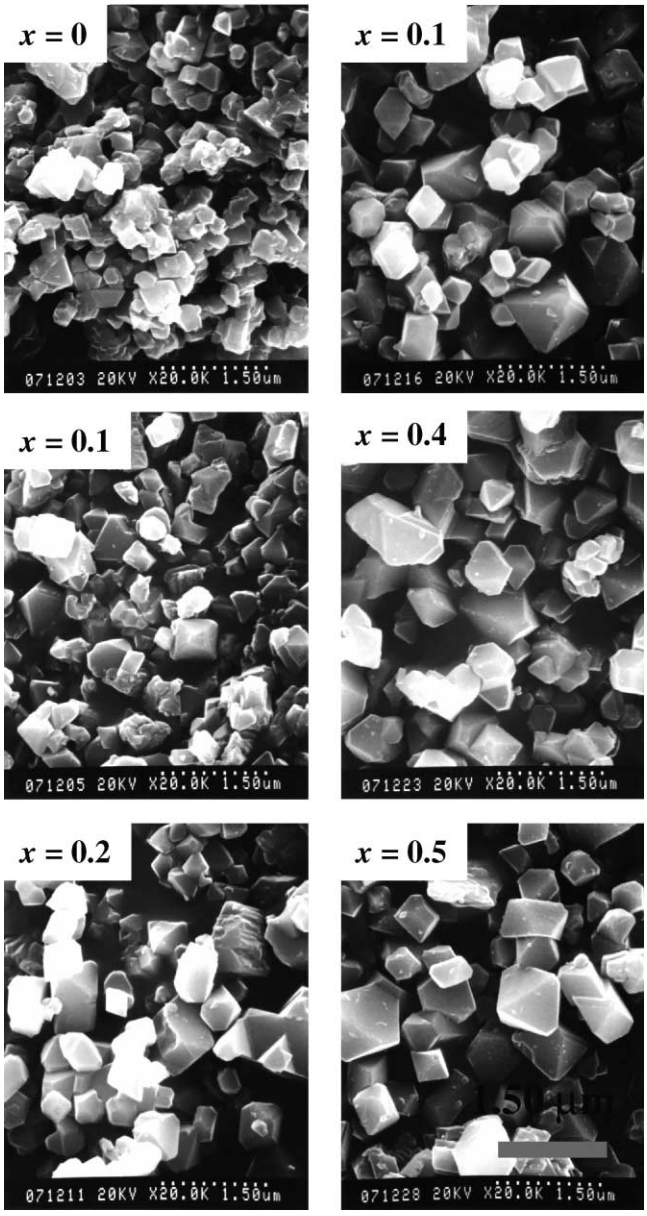

Fig. 5. Scanning electron micrographs of $Li(Mn_{2-x}Co_x)O_4$ ($0 \leq x \leq 0.5$) powders.

3.3. Mn valence analysis

The manganese L edge X-ray absorption near edge structure (XANES) spectra of $Li(Mn_{2-x}Co_x)O_4$ are shown in Fig. 7. The spectra show two broad multiple structures separated by spin-orbital splitting (Mn $2p_{3/2}$ and Mn $2p_{1/2}$). The chemical shift is caused by the change in the electrostatic energy at the Mn site, which is driven by varying the ionic valence in the compounds. The $2p_{3/2}$ absorption peaks of MnO_2 and Mn_2O_3 are marked by solid and dashed lines, respectively. The $2p_{3/2}$ peak of the $Li(Mn_{2-x}Co_x)O_4$ contains both Mn^{3+} and Mn^{4+} absorption transitions, which means that Mn^{3+} and Mn^{4+} are distributed randomly in the structure and the electron in the 3d orbitals of Mn^{3+} is localized. The chemical substitution of Co^{3+} for Mn^{3+} in $LiMn_2O_4$

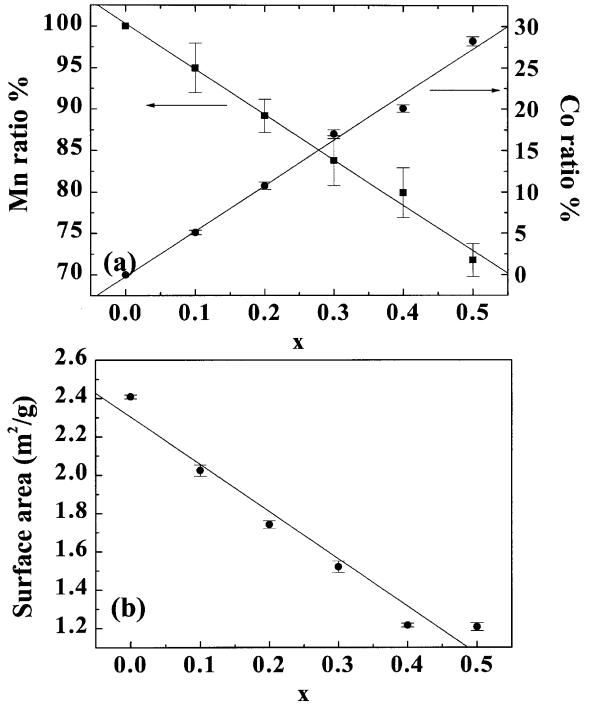

Fig. 6. (a) EDS ratio and (b) BET surface areas ($m^2\ g^{-1}$) as a function of x in $Li(Mn_{2-x}Co_x)O_4$ ($0 \leq x \leq 0.5$).

increases the Mn valence. The peak intensity of Mn^{3+} decreases compared with that of Mn^{4+} as x increases from 0 to 0.5. Liu et al. [26] have used XANES to study the valence of Mn in the $La_{1.2}Sr_{1.8-x}Ca_xMn_2O_7$ series and found a single smooth peak (not a mixture of individual Mn^{3+} and Mn^{4+} peaks), which indicates that the Mn valence remains the same as Sr is substituted by an increasing amount of Ca. Yamaguchi et al. [27] have used X-ray absorption spectro-

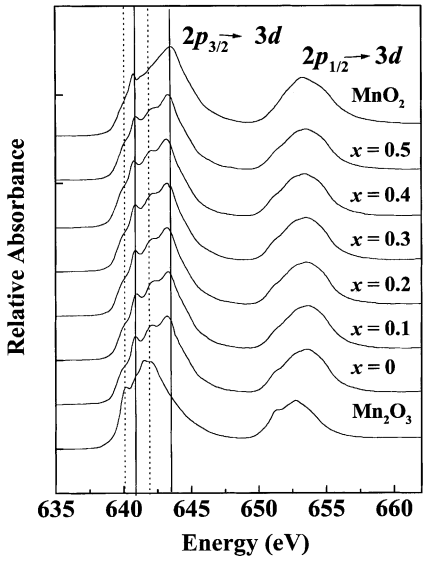

Fig. 7. Mn 2p-edge XANES spectra of samples with nominal composition $Li(Mn_{2-x}Co_x)O_4$ ($0 \leq x \leq 0.5$) and those of two standards, MnO_2 (Mn^{4+}, shown by solid line) and Mn_2O_3 (Mn^{3+}, shown by dashed line).

scopy of the Mn K edge to investigate the valence state and local structure of $LiMn_2O_4$ at 280 K. The local structure was analyzed using isotropic $Mn^{3+}O_6$ and anisotropic $Mn^{3+}O_6$ octahedra in $LiMn^{3+}Mn^{4+}O_4$. The structure exhibits local ordering of the distorted $Mn^{3+}O_6$ octahedra when the temperature is below the transition temperature. Consequently, in the cubic phase above the transition temperature, the $Mn^{3+}O_6$ octahedra are distorted by the Jahn–Teller effect, which is a local distortion without static or dynamic order. Therefore, the charge ordering process is accompanied by the presence of orbital ordering, which is the manifestation of the Jahn–Teller polaronic nature of the mobile charge above and below the transition temperature [27,28]. Thus, charge localization and a mixed valence of Mn^{3+} and Mn^{4+} are found in the system. The Mn valence of the samples from $x = 0$ to 0.5 was determined by chemical titration. The calculated average Mn valence for $x = 0$–0.5 in $LiMn_1{}^{4+}Mn_{1-x}{}^{3+}Co_x{}^{3+}O_4$ is 3.50, 3.53, 3.56, 3.59, 3.63 and 3.67, respectively, whereas the actual experimental values are 3.51 ± 0.02, 3.52 ± 0.01, 3.56 ± 0.01, 3.58 ± 0.01, 3.61 ± 0.03 and 3.68 ± 0.01, as shown in Fig. 8. Thus, it can be seen that there is a good agreement between the expected and observed values.

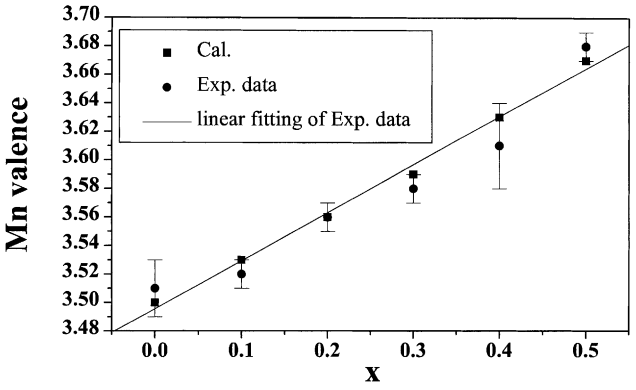

Fig. 8. Calculated and experimental Mn valence of nominal composition of $Li(Mn_{2-x}Co_x)O_4$ ($0 \leq x \leq 0.5$).

3.4. Cycling performance of spinel $Li(Mn_{2-x}Co_x)O_4$ cathode

From the chemical formula $LiMn_1{}^{4+}Mn_{1-x}{}^{3+}Co_xO_4{}^{3+}$ ($0 \leq x \leq 0.5$), the theoretical capacities based on a one-electron charge–discharge reaction are calculated to be in the range 148–96 mAh g^{-1}. The first discharge curves at the first cycle for $Li/LiMn_1{}^{4+}Mn_{1-x}{}^{3+}Co_xO_4{}^{3+}$ cells with $x =$ 0.1–0.5 together with that of $Li/LiMn_2O_4$ cell are given in Fig. 9. The initial discharge capacity of $Li/LiMn_2O_4$ ($x = 0$) is 120 mAh g^{-1}. The initial discharge capacity of $Li/Li(Mn_{2-x}Co_x)O_4$ decreases with increasing Co substitution. The capacities of $Li/Li(Mn_{2-x}Co_x)O_4$ from $x = 0.1$ to 0.5 are 105, 103, 95, 92, 85 mAh g^{-1} (as shown in Table 2). Since de-intercalation of Li^+ from the spinel structure must be electrically compensated by oxidation of Mn^{3+} to Mn^{4+}, this suggests that even for substituted spinel phases, only the amount of Mn^{3+} contributes to the charge–discharge capacity. So, the initial capacity of $Li(Mn_{2-x}Co_x)O_4$ ($0 \leq x \leq 0.5$) is limited by the initial amount of Mn^{3+} in the 16d sites. The typical charge–discharge behavior of $Li/LiMn_2O_4$ ($LiMn_1{}^{4+}Mn_1{}^{3+}Co_0{}^{3+}O_4$) at a constant current rate of $c/5$ are shown in Fig. 10. The cells were first charged to their rest voltage of 4.25 V. The removal of approximately 0.8–0.9 Li^+ from the structure occurs in two steps. Two pairs of redox peaks in the 4 V region are associated with lithium ion extraction–insertion at the 16c site [29,30]. Two peaks corresponding to the reversible two-step process for extracting Li from spinel $LiMn_2O_4$ are observed at voltages of 4.00 and 4.12 V versus Li/Li^+, respectively. During the initial cycle, the capacity loss occurs mainly at the higher voltage plateau, which may be due to the unstable two-phase structure, which exists during Li ion insertion–extraction into/from

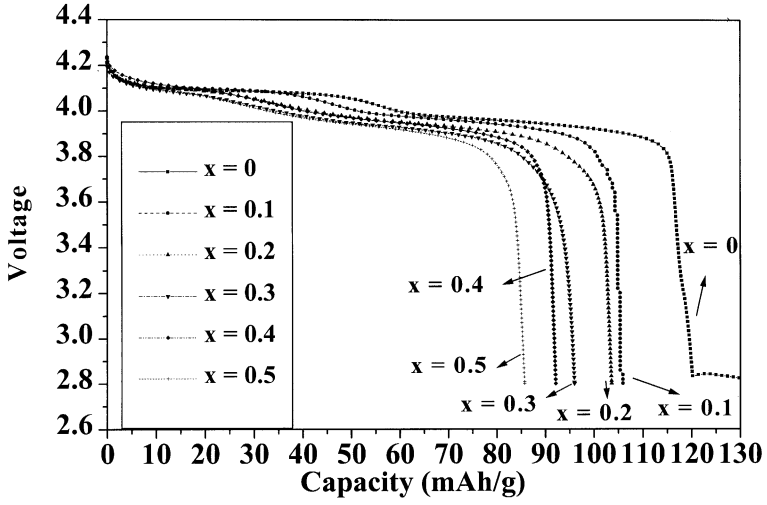

Fig. 9. Potential (V) vs. discharge capacity (mAh g^{-1}) curve obtained from first cycle for $Li(Mn_{2-x}Co_x)O_4$ ($0 \leq x \leq 0.5$). Li metal served as anode in EC(1):DMC(2)/1 M $LiPF_6$.

Table 2
Discharge capacity (mAh g^{-1}) performance of $Li(Mn_{2-x}Co_x)O_4$ ($0 \leq x \leq 0.5$) cell[a]

Sample	First cycle	15th Cycle	20th Cycle	25th Cycle
$x = 0$	120.16	94 (21%)	89.55 (25%)	87.05 (28%)
$x = 0.1$	105.37	104.86 (0.48%)	104.86 (0.48%)	103.32 (1.9%)
$x = 0.2$	103.58	102.88 (0.67%)	102.59 (1%)	101.56 (2%)
$x = 0.3$	95.97	95.75 (0.23%)	95.48 (0.5%)	89.37 (6.9%)
$x = 0.4$	92.12	91.43 (0.75%)	91.14 (1%)	90.82 (1.4%)
$x = 0.5$	85.7	85.27 (0.5%)	84.69 (1.2%)	83.8 (2.2%)

[a] Loss of discharge capacity at 15th, 20th and 25th cycle is compared with that at the first cycle. The percentage loss in capacity is given in parenthesis.

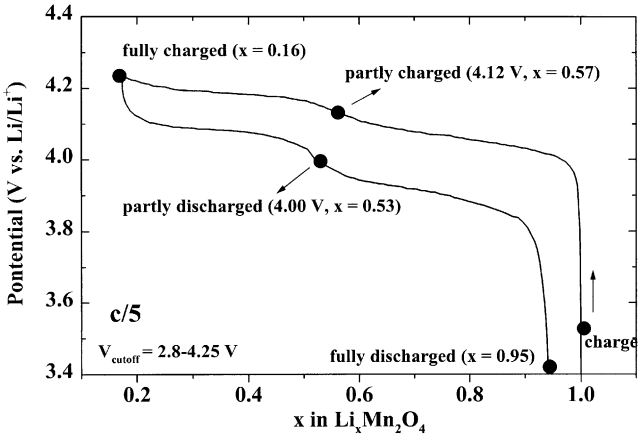

Fig. 10. Typical first charge–discharge behavior for $Li/LiMn_2O_4$ cell at a constant current rate $c/5$, $V_{cut\text{-}off}$: 2.8–4.25 V.

the spinel structure shown in Fig. 3. The first cycle charge–discharge curve versus lithium composition x of the $Li/Li_xMn_1^{4+}Mn_{0.8}^{3+}Co_{0.2}^{3+}O_4$ are presented in Fig. 11. For the range at a composition near $x = 0.6$, an anomalous charge is observed. Probably a lithium ordering–disordering process occurs during the lithium intercalation–deintercalation across $x = 0.6$ which causes a phase transformation. By increasing the substitution of Co^{3+} in Mn 16d sites, there is a decrease in the unstable two-phase region [8,9,29–32] and the curve is smooth compared with $Li/LiMn_2O_4$ (as shown in Fig. 10).

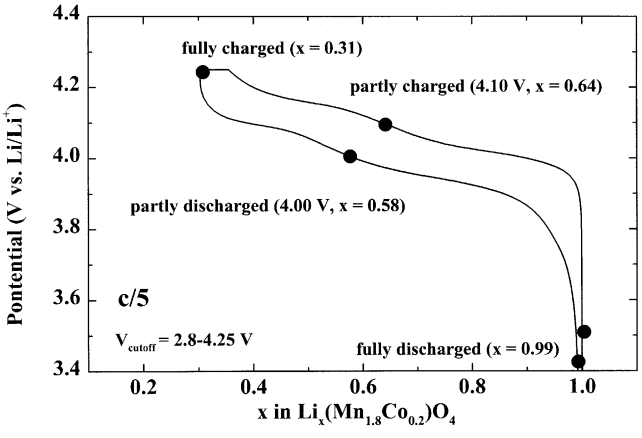

Fig. 11. Voltage vs. lithium composition x of $Li/Li_x(Mn_{1.8}Co_{0.2})O_4$ cell at first charge–discharge. Li metal served as anode in EC(1):DMC(2)/1 M $LiPF_6$ with constant current rate $c/5$ and $V_{cut\text{-}off}$: 2.8–4.25 V.

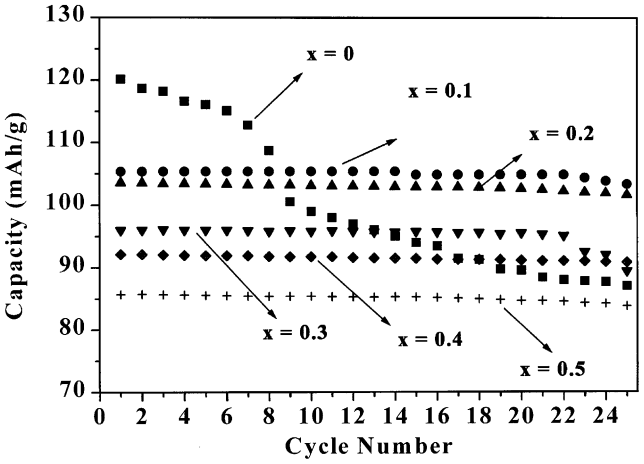

Fig. 12. Variation of discharge capacity with cycle number for $Li(Mn_{2-x}Co_x)O_4$ ($0 \leq x \leq 0.5$) cell with 1 M $LiPF_6$ in EC(1):DMC(2) electrolyte at room temperature.

The discharge capacity of $Li(Mn_{2-x}Co_x)O_4$ is shown in Fig. 12. This was obtained with the spinel cathode at a current density of $c/5$ (0.6 mA cm^{-2}). It is apparent that the discharge capacity of the doped compositions ($x = 0.1$–0.5) is more stable than that of the $LiMn_2O_4$ spinel phase, and that the capacity fading is slightly suppressed by increasing the Co content from 0.1 to 0.5. The capacity fading compared with the initial capacity before the 25th cycle is shown in Table 2. For example, the capacity loss observed with the undoped $LiMn_2O_4$ is about 25% after 20 cycles, whereas that for $x = 0.1$ and 0.2 doped spinel materials is about 0.48 and 1%, respectively. For $Li(Mn_{1.0}^{4+}Mn_{0.9}^{3+}Co_{0.1}^{3+})O_4$, the capacity of the cell maintains 98% of the initial capacity at the 25th cycle, which is nearly the same as $Li(Mn_{1.0}^{4+}Mn_{0.8}^{3+}Co_{0.2}^{3+})O_4$ (cut-off voltage 4.25–2.8 V, charge density = 0.6 mA cm^{-2}). Therefore, the spinel structure becomes more tolerant to repeated charge–discharge by doping of Co. This may be attributed to the reduction of Mn valence which gives giving rise to the suppression of the Jahn–Teller distortion via Co doping.

4. Conclusions

Undoped and doped spinels with the nominal compositions $Li(Mn_{2-x}Co_x)O_4$ with $0 \leq x \leq 0.5$ have been synthesized.

Chemical substitution of Co^{3+} for Mn^{3+} in $LiMn_2O_4$ improves the cathodic properties and the efficiency in maintaining electrochemical capacity over a large number of cycles without sacrificing initial reversible capacity and also performance at temperature below room temperature.

Acknowledgements

This research has been financially supported by the SYNergy ScienTech Corporation, and the National Science Council of the Republic of China under grant number NSC 89-2113-M-002-059.

References

[1] J.M. Tarascon, D. Guyomard, Electrochim. Acta 38 (1993) 1221.
[2] M. Winter, J.O. Besenhard, M.E. Spahr, P. Novak, Adv. Mater. 10 (1998) 725.
[3] D. Aurbach, J. Power Sources 89 (2000) 206.
[4] M.M. Thackeray, W.I.F. David, P.G. Bruce, J.B. Goodenough, Mater. Res. Bull. 18 (1983) 461.
[5] C. Delmas, M. Menetrier, L. Croguennec, S. Levasseur, J.P. Peres, C. Pouillere, G. Prado, Int. J. Inorg. Mater. 1 (1999) 11.
[6] J.B. Goodenough, Solid State Ionics 69 (1994) 184.
[7] M.M. Thackeray, J. Electrochem. Soc. 142 (1995) 2558.
[8] Y. Xia, N. Kumada, M. Yoshio, J. Power Sources 90 (2000) 135.
[9] S. Mukerjee, T.R. Thurston, N.M. Jisrawi, X.Q. Yang, J. McBreen, M.L. Daroux, X.K. Xing, J. Electrochem. Soc. 145 (1998) 466.
[10] W. Liu, K. Kowal, G.C. Farrington, J. Electrochem. Soc. 145 (1998) 459.
[11] K. Miura, A. Yamada, M. Tanaka, Electrochim. Acta 41 (1996) 249.
[12] A.D. Robertson, S.H. Lu, W.F. Averill, W.F. Howard, J. Electrochem. Soc. 144 (1997) 3500.
[13] A.D. Robertson, S.H. Lu, W.F. Averill, W.F. Howard, J. Electrochem. Soc. 144 (1997) 3505.
[14] G. Pistoia, A. Antonini, R. Rosati, C. Bellitto, G.M. Ingo, Chem. Mater. 9 (1997) 1443.
[15] Y. Ein-Eli Jr., W.F. Howard, J. Electrochem. Soc. 144 (1997) L205.
[16] L. Sanchez, J.L. Tirado, J. Electrochem. Soc. 144 (1997) 1939.
[17] L. Guohua, H. Ikuta, T. Uchida, M. Wakihara, J. Electrochem. Soc. 143 (1996) 178.
[18] A.D. Pasquier, A. Blyr, P. Courjal, D. Larcher, G. Amatucci, B. Gerand, J.M. Tarascon, J. Electrochem. Soc. 146 (1999) 428.
[19] A.C. Larson, R.B. von Dreele, Generalized Structure Analysis System, Los Alamos National Laboratory, Los Alamos, NM, 1994.
[20] M.J. Katz, R.C. Charke, W.F. Nye, Anal. Chem. 28 (1956) 507.
[21] H. Berg, K. Goransson, B. Nolang, J.O. Thomas, J. Mater. Chem. 9 (1999) 2813.
[22] R.D. Shannon, Acta Crystallogr. A 32 (1976) 751.
[23] C.H. Shen, R.S. Liu, R. Gundakaram, H.S. Sheu, J. Chem. Soc., Dalton Trans. (2001) 37.
[24] C. Masquelier, M. Tabuchi, K. Ado, R. Kanno, Y. Kobayashi, Y. Maki, O. Nakamura, J.B. Goodenough, J. Solid State Chem. 123 (1996) 255.
[25] P. Arora, B.N. Popov, R.E. White, J. Electrochem. Soc. 145 (1998) 807.
[26] R.S. Liu, C.H. Shen, J.G. Lin, C.Y. Huang, J.M. Chen, R.G. Liu, J. Chem. Soc., Dalton Trans. (1999) 623.
[27] H. Yamaguchi, A. Yamada, H. Uwe, Phys. Rev. B 58 (1998) 8.
[28] J. Rodriguez-Carvajal, G. Rousse, C. Masquelier, M. Hervieu, Phys. Rev. Lett. 81 (1998) 4660.
[29] O.S. Kwon, M.S. Kim, K.B. Kim, J. Power Sources 81/82 (1999) 510.
[30] B. Ammundsen, J. Roziere, M.S. Lsalm, J. Phys. Chem. B 101 (1997) 8156.
[31] J.H. Lee, J.K. Hong, D.H. Jang, Y.K. Sun, S.M. Oh, J. Power Sources 89 (2000) 7.
[32] D. Song, H. Ikuta, T. Uchida, M. Wakihara, Solid State Ionics 117 (1999) 151.